Article

Unusual Enhancement of the Optical Depth on the Continental Shelf Depth Latitudinal Variation in the Stratospheric Polar Vortex

Ziqiang Xu [1,2], Yuanyuan Qian [1,2], Taiping Yang [1], Fuying Tang [1,2], Yuhan Luo [1] and Fuqi Si [1,*]

1   Key Laboratory of Environmental Optics & Technology, Anhui Institute of Optics and Fine Mechanics, Hefei Institutes of Physical Science, Chinese Academy of Sciences, Hefei 230031, China; xzqxzq@mail.ustc.edu.cn (Z.X.); yyqian@aiofm.ac.cn (Y.Q.); tpyang@aiofm.ac.cn (T.Y.); fytang@aiofm.ac.cn (F.T.); yhluo@aiofm.ac.cn (Y.L.)
2   University of Science and Technology of China, Hefei 230026, China
*   Correspondence: sifuqi@aiofm.ac.cn

Abstract: The Antarctic ozone hole has attracted attention concerning global climate change. Breakthroughs regarding ozone observation methods and the formation principles of ozone holes have occurred. This study compared the slant column ozone obtained from SCanning Imaging Absorption SpectroMeter for Atmospheric CHartographY (SCIAMACHY) Level 1 optical spectroscopy data processed by QDOAS software with that reconstructed from SCIAMACHY Level 2 ozone data using geographic information to obtain the optical depth coefficients. The global distribution of optical depth coefficients reveals latitudinal homogeneity, whereas the distribution of coefficients in the polar regions reveals heterogeneity. This heterogeneity has an annual variation pattern, alternating between strong and weak distributions in the Arctic and Antarctic regions. It is most evident in the Palmer Peninsula of Antarctica, where the optical depth coefficients were significantly higher than those of the surrounding regions at the same latitude. This analysis excluded the atmospheric pressure influence and suggested the influence of the continental shelf depth. The protrusion of the continental shelf depth changes the optical depth coefficients owing to the geographical proximity of the Antarctic Palmer Peninsula to South America, which separates the Atlantic and Pacific Oceans in an east–west direction.

Keywords: stratospheric ozone; optical depth coefficients; polar vortex; limb viewing; differential optical absorption spectroscopy; tomography

1. Introduction

Countries have gradually banned the production and sale of ozone-depleting substances after signing the Montreal Protocol in 1987 [1]. This has led to the gradual recovery of stratospheric ozone. The ozone layer is slowly recovering to the levels seen before 1980 [2]. Temperature effects on chemical reaction rates and the response of stratospheric circulation to greenhouse gas concentrations affect ozone recovery [3,4]. Chlorofluorocarbons [5,6] and bromine-containing reaction intermediate emissions [7] also have significant impacts [8]. The effects of various variables on the vertical distribution of ozone must be continuously observed using limb satellites [9] in the context of changing atmospheric thermodynamics, dynamics, and chemistry [10]. The polar vortex acts as a barrier to ozone transport in polar regions where the climatic conditions differ from other regions [11]. Polar stratospheric cloud formation contributes to ozone depletion and the eventual formation of ozone holes [12,13].

Antarctic polar vortices typically form in April [14] and subside during November and December [15–17]. Thermal radiative cooling during the polar night triggers the massive formation of polar stratospheric clouds [12,13]. Solar radiation in the polar region causes

molecular chlorine to undergo photolysis, forming chlorine radicals that enter the catalytic cycle of ozone destruction. Antarctic ozone holes are usually observed from August to November and cover an area of up to 30 million km^2 [18]. The term "polar vortex" refers to three different atmospheric features: the stratospheric polar vortex, the tropospheric polar vortex (which has strong winds surrounding the poles), and smaller-scale tropospheric polar vortex regions located at the poles [17]. The stratospheric polar vortex is most likely characterized by a strong circumpolar westerly wind [19,20] that reaches a maximum at approximately 60° latitude [21,22]. The Antarctic and Arctic have polar eddies; however, they cause different ozone distributions owing to differences between the Northern and Southern Hemispheres [23]. Antarctic ozone holes annually appear; however, the Arctic cannot form long-term ozone holes [2]. This phenomenon is widely believed to be because of the formation of strong polar eddies on the Antarctic continent that impede ozone transport from the equator to polar regions [24,25]. This is usually coupled with stratospheric clouds formed by strong polar vortices that bring halogenic elements into the stratosphere and accelerate ozone depletion [26]. Eddies formed in the Antarctic region can be observed regarding temperature and pressure [27]. This study introduces a new observation method for polar eddies and interprets them from the perspective of optical depth coefficients. This unique perspective brings together different perspectives and understandings by linking shelf protrusions to eddy formation.

Our study is based on two well-established approaches. The first approach retrieves the stratospheric ozone profile from optical spectrograph data from limb satellites. The modified onion-peeling approach (MOP) was applied to OSIRIS limb observations for the first time using the transmission spectrum of the low tangent height and the reference spectrum of the stratopause to reflect the vertical profile of multiple ozone layers [28]. UV-band limb L1 data was used from the SCanning Imaging Absorption SpectroMeter for Atmospheric CHartographY (SCIAMACHY) to successfully invert the vertical ozone profile of the stratosphere by combining radiation normalization and optimal estimation (OE) [29]. The second method derives gas profiles in an open atmosphere using differential optical absorption spectroscopy (DOAS) [30]. Tomographic reconstruction chamber measurements of two-dimensional trace gas distributions were initially performed using infrared light absorption in the 1990s, and the velocity and spatial resolution have improved since then [31].

Meanwhile, long-path instruments that were developed to measure the horizontal distribution of 2D emission plumes or trace gases from road traffic are more suitable for tomographic applications [32], as demonstrated by laboratory validation activities. Furthermore, the 2D distribution of emission plumes from a power plant was measured by passive instruments onboard an aircraft and the location and emissions of atmospheric emission plumes were estimated through numerical studies [33]. It is possible to determine polar optical depth coefficients using these techniques [34,35].

Previous studies have examined Antarctica's ozone hole and polar vortex, and various parameters have been comprehensively considered, such as PV (potential vorticity) and temperature gradient. However, no research has evaluated the impact of the protrusion of the continental shelf depth on the polar vortex. The optical depth coefficients proposed in this study can quantify the impact of the latitudinal change in the continental shelf depth on the polar vortex. The optical depth coefficients can be considered a parameter in future research's current model of the polar vortex and the polar ozone hole.

2. Materials and Methods

The method proposed in this study obtains the optical depth coefficients based on the L1 and L2 data of limb satellites. Persuasiveness was enhanced using official L2 ozone data instead of individual inversions of the stratospheric ozone vertical profile [36]. Official L2 ozone data were modelled using Earth curvature geographic information to obtain the ozone number density on the geometric path (the geometric path refers to the physical, straight-line path that light would take in a vacuum or uniform medium). The L1 data for

each height of limb scanning were processed using QDOAS to obtain the ozone number density on the optical path (the optical path takes into account the medium through which light is traveling). The ratio between the ozone number density on optical path and that on the geometric path is the optical depth coefficients.

Limb observations substantially improved the study of the vertical fine ozone structure [37]. They also accurately describe the fine vertical structure of polar eddies. An in-orbit satellite observes the radiation that the atmosphere transmits in the horizontal direction. It uses the DOAS algorithm to calculate the slant column ozone on the optical path. The slant ozone column on the geometric path can be constructed by combining the vertical ozone profile with real geographic information. The vertical structure profile of ozone directly adopts the official L2 ozone products to increase persuasiveness. The geometry and auxiliary data for the limb observations are briefly described below.

The SCIAMACHY limb observation scans the structure of the stratified atmosphere in the horizontal direction. It simultaneously records the emission and scattering spectra of the atmosphere (indicated by the horizontal blue line in Figure 1). Different scanning lines of sight pass through different layers, and the scanning of the atmosphere usually starts from the height of the ground surface and scans upward at a certain angle to obtain data from different atmospheric layers. The last scan points to deep space to record the effect of dark currents on the data for subsequent correction. The motor returns to its original position after completing one scan before the next round of scanning. The single scatter (SS) accounts for the largest proportion of radiation sources, with multiple scatter (MS) and albedo scatter (AS) having the least influence. Albedo scatter depends on the properties of the surface, so global albedo lookup tables are used in the ozone retrieval process to improve accuracy. SCIAMACHY was one of ten scientific instruments aboard the ENVISAT environmental satellite. The satellite was launched into a sun-synchronous orbit at an altitude of approximately 800 km, an inclination of $98.55°$, and an ascent node at 10:00 GMT on 1 March 2002. Bovensmann et al. (1999) reported detailed information about the SCIAMACHY instrument [38].
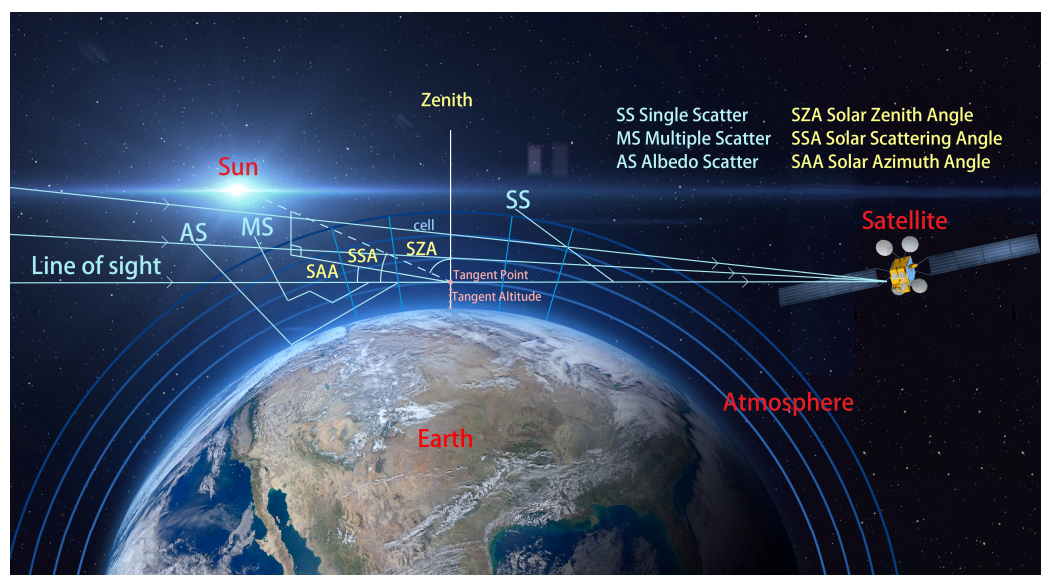
Figure 1. Limb observation geometry. AS, albedo scatter; MS, multiple scatter; SS, single scatter; SAA, solar azimuth angle; SSA, single scattering angle; SZA, solar zenith angle.

The mature DOAS technology in this study can be directly applied to obtain the slant ozone column along an optical path. The QDOAS developed by the Belgian Royal Institute for Space and Aeronomy (BIRA-IASB) was used to obtain the ozone number density, and the parameter settings can be publicly communicated [39]. The real ozone column on the geometric path was reconstructed based on geographic information using the vertical

ozone profile published by the European Space Agency (ESA). The ratio between the ozone number density on the optical path and that on the geometric path is the optical depth coefficient of the current height.

2.1. DOAS

The DOAS method is based on the Lambert–Beer law and obtains the concentration of trace gases via characteristic light intensity absorption [40]. The Lambert–Beer law and its derivation are presented below:

$$In\frac{I^*(\lambda)}{I_0(\lambda)} = -\sum_k \left(\delta^*{}_k(\lambda)\cdot c_k\cdot L\right) = -\sum_k \left(\delta^*{}_k(\lambda)\cdot C_k\right) \tag{1}$$

where $I^*(\lambda)$ is the measured light intensity, $I_0(\lambda)$ is the original light intensity, $\delta^*{}_k(\lambda)$ is the absorption cross section of trace gases k, c_k is the concentration of trace gases k, L is the optical path length, C_k is the slant column of trace gases k, $In\frac{I^*(\lambda)}{I_0(\lambda)}$ is the optical density, and λ is the wavelength. The least-squares fitting of Equation (1) yields the $C_{j,qdoas}$ of ozone gas of j-th line of sight (LOS) [41].

In this study, the ozone differential slant column density (DSCD) was retrieved from the QDOAS software developed by the BIRA-IASB. The inversion wavelength range was 320–340 nm and the NO_2, O_3, O_4, HCHO, BrO, and ring cross sections were considered in the DOAS fitting (Table 1).

Table 1. Detailed parameters of differential optical absorption spectroscopy (DOAS) fittings.

Parameters	Settings
Fitting Interval	320–340 nm
Polynomial	Order 5
Cross sections	
O_3	223 K, 243 K [42]
NO_2	298 K [43]
O_4	293 K [44]
HCHO	297 K [45]
BrO	223 K [46]
Ring	Calculated using QDOAS

For the reference spectrum, 50 km-slice high spectra were used to accurately determine the effect of stratospheric ozone. The effect of short-term evolution on the stratosphere can be ignored using this method since the stratospheric ozone was stable and on a large scale. Here is an example, the tangent height was 30 km after taking the spectral fitting of 5.994°N and 126.927°E at 1:43:58.7 on 1 July 2011 (Figure 2). The inverted ozone DSCD was 5.42×10^{19} molec/cm^2 (DSCD error 6.73×10^{17} molec/cm^2), and the spectral fitting residual's root mean square (RMS) was 8.78×10^{-3}. Other trace gases have no effect on the results, so they are not shown in the picture. In the QDOAS software, the output is high-pass filtered. As a result, negative values appear on the ordinate axis in Figure 2b–d.

The above is a point at a tangent height of 30 km, and the same method can be used to calculate all of the data at different tangent heights on the entire vertical profile (Figure 3a).
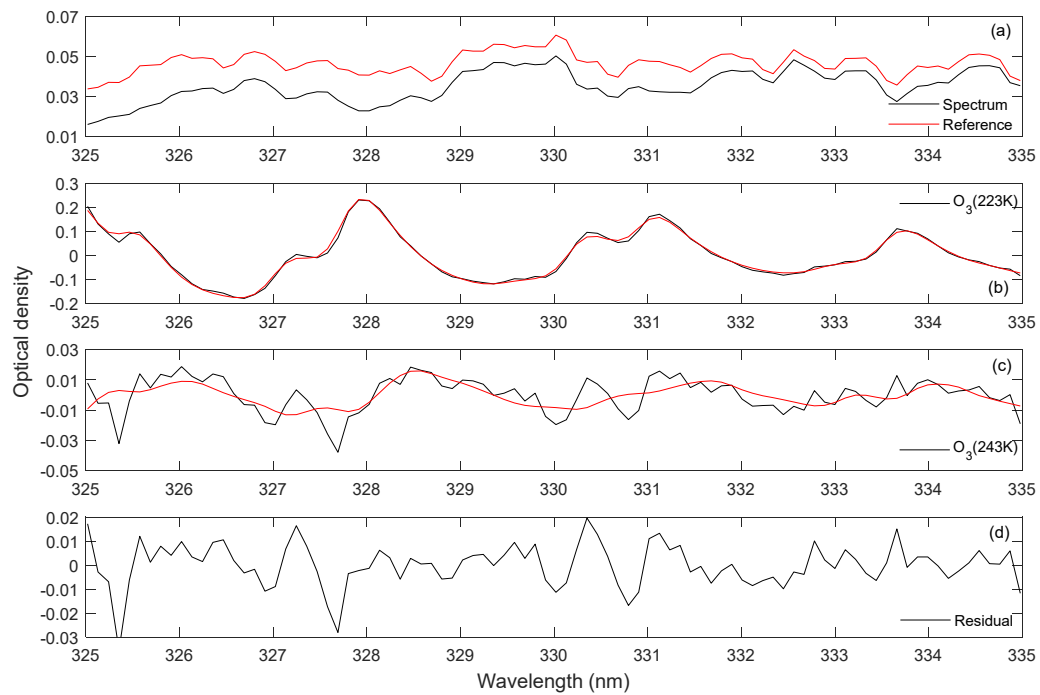
Figure 2. Example of ozone differential slant column density (DSCD) inversion at 01:43:58.7 on 1 July 2011, showing (**a**) measured (black line) and reference (red line) spectra, (**b**) measured (black line) and fitted (red line) O_3 (223 K) optical density, (**c**) measured (black line) and fitted (red line) O_3 (243 K) optical density, and (**d**) remaining residuals from the DOAS fit.
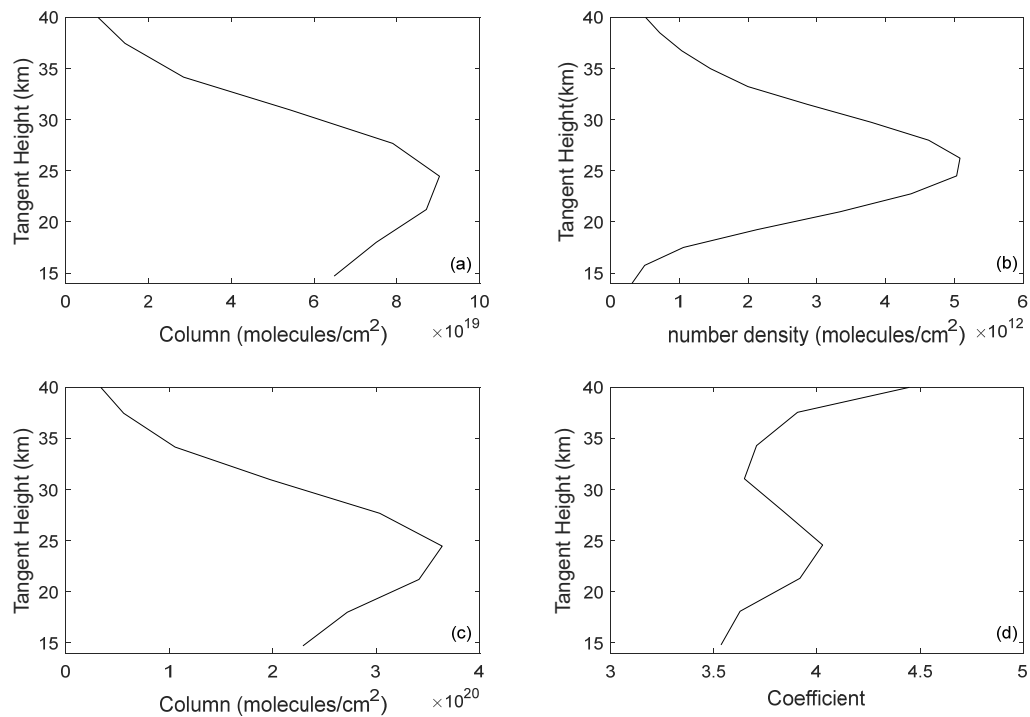
Figure 3. Calculation steps of the optical depth coefficients. (**a**) Line-of-sight slant ozone density obtained by the DOAS algorithm. (**b**) SCIAMACHY L2 ozone product. (**c**) Line-of-sight slant ozone density obtained by reconstructing geographic information. (**d**) Optical depth coefficients.

2.2. Reconstructing Geographic Information to Calculate Optical Depth Coefficients

The above method calculates the slant ozone column on optical path. There are no corresponding official data; therefore, a unique technology is required to convert the official data. Figure 3 shows a schematic summarizing the slant ozone column over the cells through which the line of sight passes. The cell is constructed based on the curvature information of the Earth. The height of the cell is 3 km, the width is 100 km, and it is in the shape of an arc. Fill each cell according to the value of each height of ozone and accumulate these cells to obtain the slant ozone column on the geometric path. The official ozone vertical profile was converted into the slant ozone column on the geometric path (Figure 3b,c). The slant column ozone on the geometric path can be expressed in discrete form for a single LOS:

$$C_{j,reconstruction} = \sum_i n_i S_{i,j},\tag{2}$$

where $C_{j,reconstruction}$ represents the reconstructed ozone slant column density of the j-th LOS, n_i is the slant ozone number density of cell i in the atmospheric grid, $S_{i,j}$ is the average optical path of the jth LOS through cell i, $S_{i,j} = \alpha_{i,j}L_{i,j}$, $\alpha_{i,j}$ is the optical depth coefficient of the jth LOS through cell i, and $L_{i,j}$ is the geometric path (Figure 4).
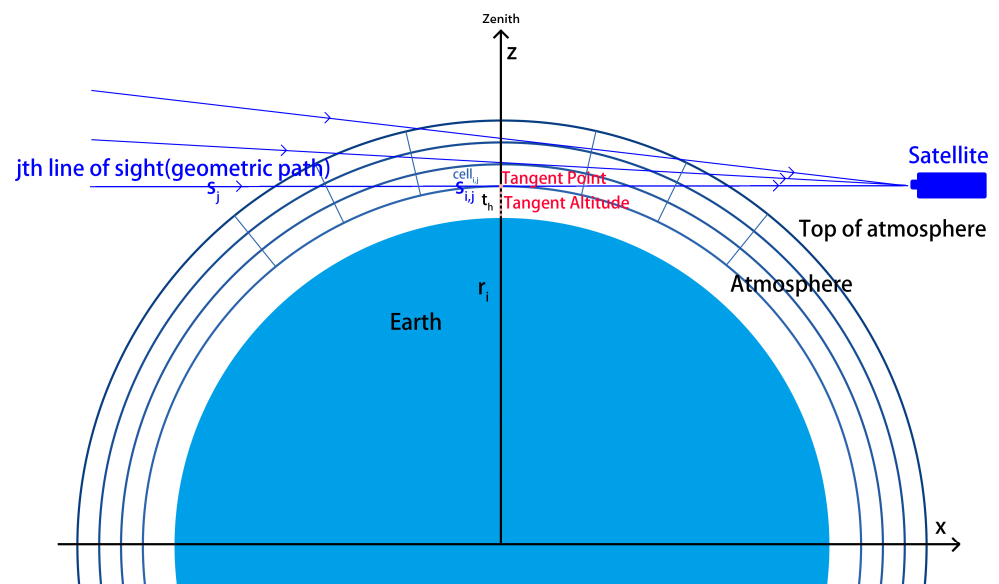
Figure 4. Limb observation schematic.

It is not feasible to solve the optical depth coefficient ($\alpha_{i,j}$) using this method owing to the difficulty in calculating $S_{i,j}$. It is feasible to use the ratio of the slant ozone density obtained by the DOAS algorithm on the optical path to the slant ozone density on the geometric path obtained by geographic information reconstruction as a solution to calculate α_j (the average value of $\alpha_{i,j}$ of the jth LOS). The lookup table for different months worldwide was obtained using the following formula [42]:

$$\alpha_j = \frac{C_{j,qdoas}}{\sum\limits_i n_i L_{i,j}},\tag{3}$$

where $C_{j,qdoas}$ is obtained by the DOAS algorithm on the optical path of the jth LOS using QDOAS. The calculated optical depth coefficient (α_j) is shown in Figure 3d.

2.3. Feasibility of the SCIATRAN Sensitivity Analysis

This study is focused on the stratospheric ozone, calculating the effect of tropospheric parameters on the stratosphere. Convection between the upper and lower layers was

notably weak owing to the stability of the stratosphere, and there is a tropopause barrier between the stratosphere and troposphere. Theoretically, changes in tropospheric parameters do not significantly impact stratospheric results. SCIATRAN (SCIAmachy TRANsmission model) is a radiative transfer model that allows for the interpretation of remote sensing data. It is designed to model and analyze how sunlight interacts with Earth's atmosphere. Changing various parameters of the SCIATRAN model by mimicking tropospheric disturbances (including cloud height, cloud fraction, visibility, and nitrogen dioxide concentration) does not have a large effect on stratospheric parameters [43,44].

2.3.1. Clouds

Cloud height parameters were set to 1, 5, and 10 km, and cloud optical depth parameters were set to 0.05, 0.5, and 5 in the SCIATRAN model. The slant column ozone affected by these parameters is shown in Figure 5, where the radiance at a 21.2 km tangent height varies with the wavelength (Figure 6a) and the radiance at 330 nm varies with the tangent height (Figure 6b).
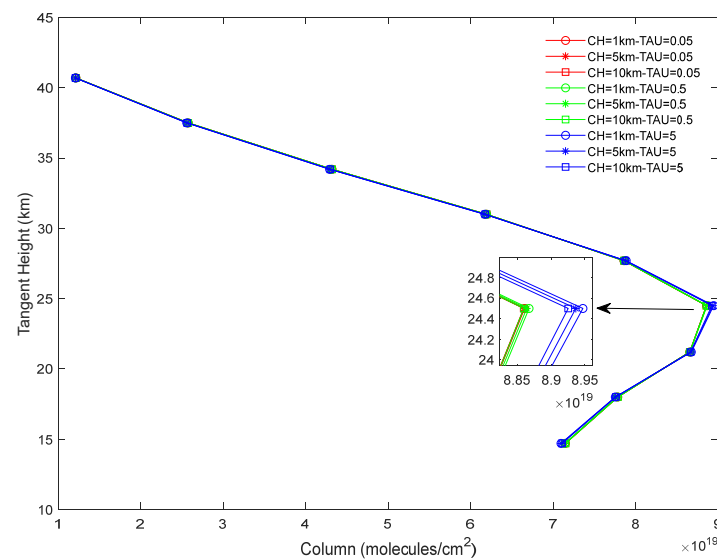
Figure 5. Influence of cloud parameters on the calculated slant ozone column.
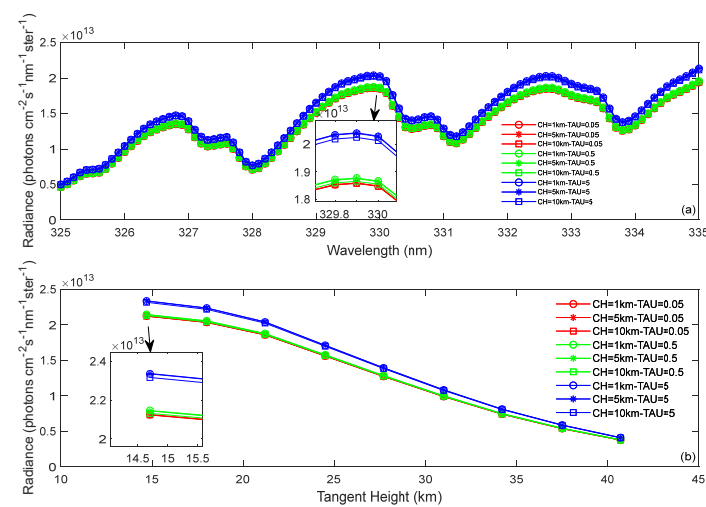
Figure 6. The influence of cloud parameters on the radiation value. (**a**) Simulated radiance change with wavelength (tangent height = 21.2 km). (**b**) Simulated radiance change with tangent height (330 nm).

The influence of cloud height and optical depth gradually decreased as the altitude increased (Figures 5 and 6). Different wavelengths exhibited different absorption characteristics, and the peak exhibited a more evident change than the trough. Overall, the cloud change had no significant effect on the final result and the 1% error for a large cloud optical depth could be disregarded.

2.3.2. Aerosols

Aerosols are also a source of error that affects the stratospheric ozone concentrations [45]. This study used the band from 325 to 335 nm; therefore, the influence was theoretically relatively small. This study focused on the boundary layer visibility and tropospheric visibility. The boundary layer visibility was set to 2, 5, 10, 23, and 50 km, and the troposphere visibility was set to 23 and 50 km. The other parameter settings are listed in Table 2. The slant ozone column under the influence of these parameters is shown in Figure 7, where the radiance at a 21.2 km tangent height varies with the wavelength (Figure 8a) and the radiance at 330 nm varies with the tangent height (Figure 8b).

Table 2. Detailed parameters of SCIATRAN.

Parameters	Settings
Aerosol optical depth scaling	1
Season	Spring/summer
Boundary layer	
Aerosol type	Maritime
Visibility	2 km/5 km/10 km/23 km/50 km
Humidity	80%
Troposphere	
Visibility	23 km/50 km
Humidity	80%
Stratosphere	
Aerosol loading	Background
Aerosol type	Background
Mesosphere	
Aerosol loading	Normal mesosphere
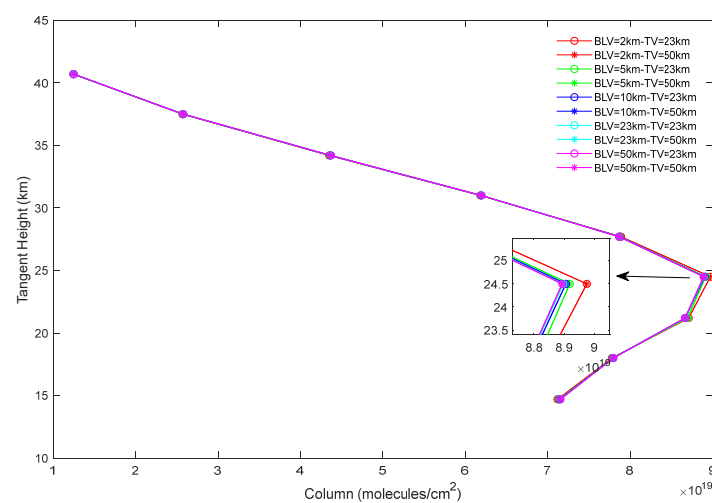
Figure 7. Influence of aerosol parameters on the calculated slant ozone column.
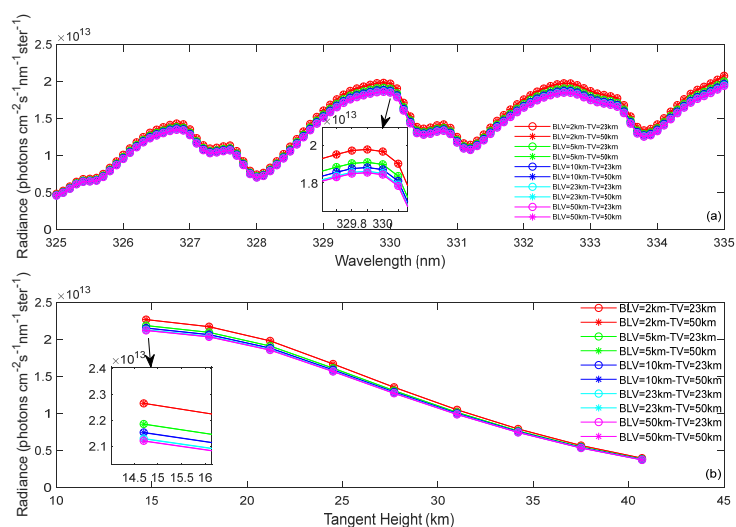
Figure 8. The influence of aerosol parameters on the radiation value. (**a**) Simulated radiance change with wavelength (tangent height = 21.2 km). (**b**) Simulated radiance change with tangent height (330 nm).

The visibility of the boundary layer does not influence the slant ozone column density (Figure 7). The error was close to 1% for the 2 km boundary layer visibility, and the troposphere visibility did not significantly change. Therefore, the results were not significantly affected. In general, there is an error of approximately 1% when the visibility of the boundary layer is 2 km, and the error in the final result can be disregarded when the visibility of the boundary layer was >5 km. The effect of tropospheric visibility on the results was negligible. The visibility within the boundary layer does not have a significant impact on the radiance across varying tangent heights. (Figure 8). Since it is a DOAS algorithm, changes in radiance have little effect on the results.

2.3.3. NO$_2$

The wavelength range of 325 to 335 nm only simulates and discusses the influence of NO$_2$ on the results when considering atmospheric absorption gases such as NO$_2$, O$_4$, and BrO. The prior profiles were set at multipliers of 0.2, 0.5, 2, and 5 times using the SCIATRAN model. The slant ozone column under the influence of different NO$_2$ contents is depicted in Figure 9, where the radiance at a 21.2 km tangent height varies with the wavelength (Figure 10a) and the radiance at 330 nm varies with tangent height (Figure 10b).
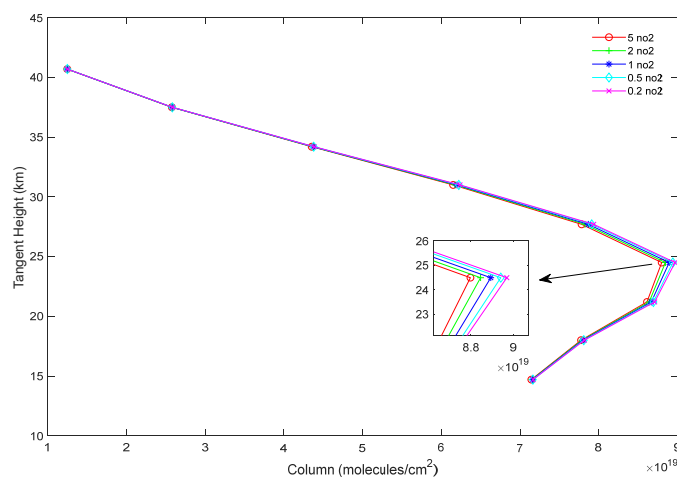
Figure 9. The influence of NO$_2$ parameters on the calculated slant ozone column.
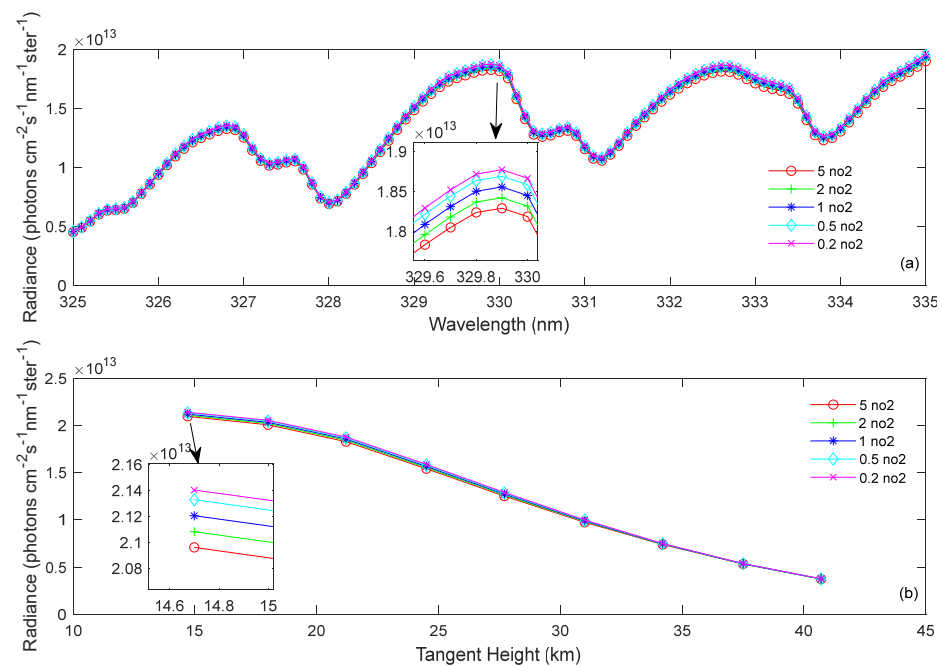
Figure 10. The influence of NO_2 parameters on the radiation value. (**a**) Simulated radiance change with wavelength (tangent height = 21.2 km). (**b**) Simulated radiance change with tangent height (330 nm).

Figure 9 indicates that the change in NO_2 concentration had no notable effect on the calculated slant ozone column density and only exhibited a weak effect when the overall concentration was increased or decreased five times; however, such extreme cases are unlikely to occur. An increase in the NO_2 concentration results in a slight decrease in the slant column ozone. The change in the trace gas NO_2 concentration did not exceed 1% of the slant ozone column, the selected band was less affected, and the band range was reasonable. The NO_2 concentration does not exert an influence on the radiance across varying tangent heights. (Figure 10). Given the application of the DOAS algorithm, slight variations in radiance have minimal influence on the results.

3. Results and Discussion

3.1. Global Optical Depth Coefficients (α_j)

The global coefficient distribution map was constructed using the above method, and the resulting zonal distribution was homogeneous (Figures 11–14). However, this zonal homogeneity was broken in the Arctic and Antarctic circles and the coefficient distribution changes with the continental shelf depth [46]. The coefficients were low in the North Atlantic Ocean in the Northern Hemisphere and increased in Greenland and further north. Meanwhile, the coefficients were distributed homogeneously in the Antarctic continental margin in the Southern Hemisphere. However, the coefficients in the Palmer Peninsula abnormally increase. The abnormal increase in optical depth coefficients was assumed to be related to atmospheric pressure; however, the change in optical depth coefficients did not match the shift in tropopause pressure from the analysis of the public tropopause pressure data from the National Oceanic and Atmospheric Administration (NOAA). Therefore, the influence of atmospheric pressure was excluded (Figure A3). The region where the coefficient exhibited latitudinal variations aligned with the changes in the depth of the continental shelf (Figure A4); therefore, the change in the continental shelf depth can explain the change in optical depth coefficients. Finally, the previous year's (2010) data were used to verify that the connection between the optical depth coefficients and the continental shelf depth; this was useful.
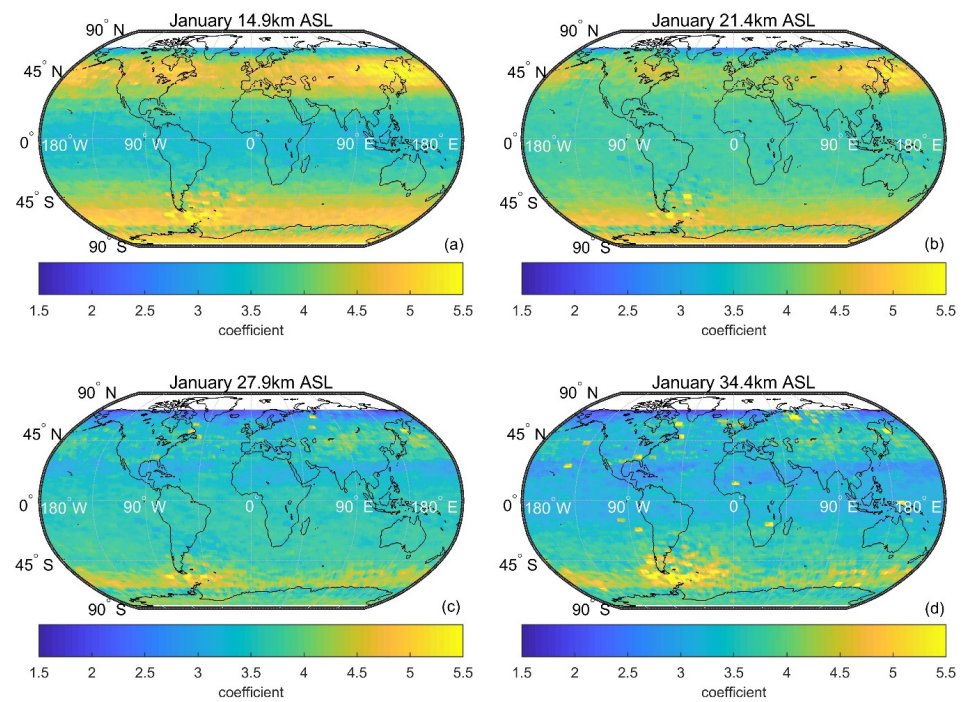
Figure 11. Optical depth coefficients with different tangent heights in January 2011. (**a**) 14.9 km, (**b**) 21.4 km, (**c**) 27.9 km, and (**d**) 34.4 km above sea level (ASL).
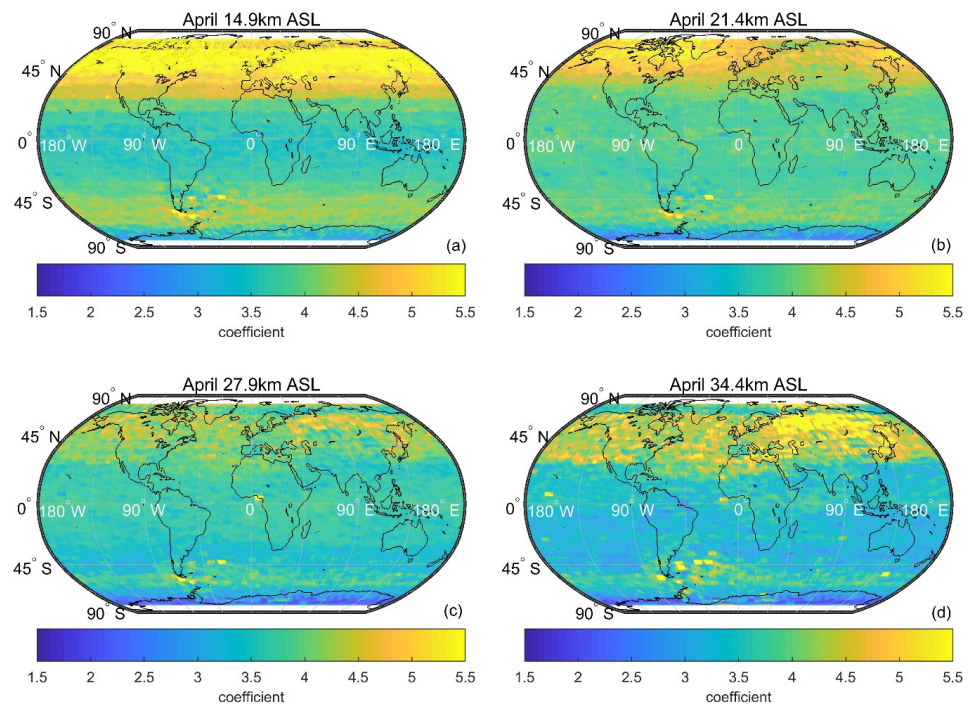
Figure 12. Optical depth coefficients with different tangent heights in April 2011. (**a**) 14.9 km, (**b**) 21.4 km, (**c**) 27.9 km, and (**d**) 34.4 km ASL.
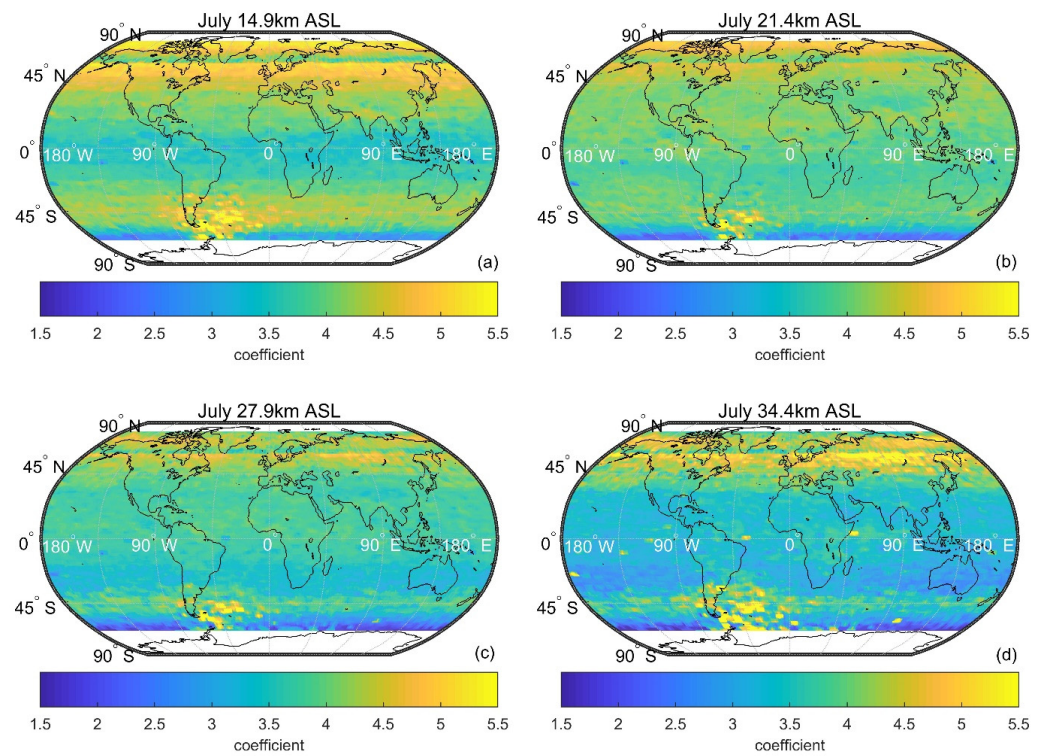
Figure 13. Optical depth coefficients with different tangent heights in July 2011. (**a**) 14.9 km, (**b**) 21.4 km, (**c**) 27.9 km, and (**d**) 34.4 km ASL.
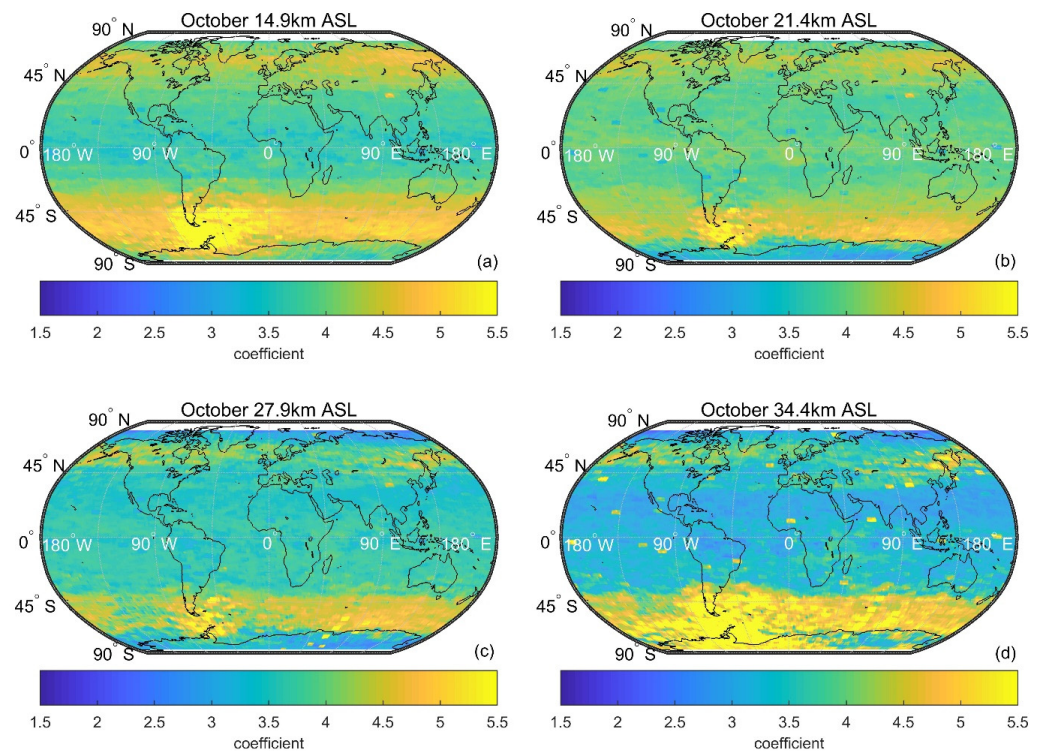
Figure 14. Optical depth coefficients with different tangent heights in October 2011. (**a**) 14.9 km, (**b**) 21.4 km, (**c**) 27.9 km, and (**d**) 34.4 km ASL.

Higher latitudes characterize the distribution of global optical depth coefficients more heterogeneously than low latitudes. At low latitudes, the distribution of coefficients is homogeneous in the latitudinal direction; however, the latitudinal homogeneity worsens

at high latitudes. The optical depth coefficients for different seasons and heights also had different distribution characteristics. The coefficients of mid-to-high latitudes in the Northern Hemisphere were relatively high in the first semester of the year. Meanwhile, the coefficients of mid-to-high latitudes in the Southern Hemisphere were relatively high in the second semester of the year. The distributions of the coefficients at different altitudes were also different in the stratosphere, and the coefficients in the lower stratosphere were higher than those in the upper stratosphere. Interestingly, the South Pacific anomaly impacted the SCIAMACHY data; therefore, the data reliability for the Atlantic region east of Argentina was low [47].

Figure 11 depicts a map of the optical depth coefficients for January. The coefficients in Southwest Greenland increased by less than 5% compared with other areas at the same latitude. The coefficients in Northern Japan increased by about 20% compared with other areas at the same latitude. These distribution features disappear in the upper stratosphere. The Palmer Peninsula and South America near the Antarctic have higher coefficients (about 30%) than the surrounding ocean areas and are unaffected by altitude in the Southern Hemisphere. Figure 12 shows a map of the optical depth coefficients for April. The coefficients in Southwest Greenland increased by about 20% compared with other areas at the same latitude. The coefficients in Northern Japan increased by less than 10% compared with other areas at the same latitude.

The Northern Hemisphere characteristics were enhanced in April compared with January. Furthermore, the area where the coefficients increased in the Palmer Peninsula decreased in the Southern Hemisphere. The Southern Hemisphere characteristics in April were weakened compared with January. The Northern Hemisphere optical depth coefficient plot further weakens in July compared with April, and the Southern Hemisphere features are strengthened compared with April (Figure 13). The Northern Hemisphere features disappear, whereas the Southern Hemisphere features are further strengthened in October compared with July based on a map of the optical depth coefficients (Figure 14). In general, the Northern Hemisphere features are not year-round and mainly appear in the lower stratosphere; the Southern Hemisphere features exist throughout the year and the entire stratosphere is present. Finally, the Southern Hemisphere features are more pronounced than the Northern Hemisphere features.

3.2. Antarctic Optical Depth Coefficient (α_j) Analysis

Previously, we described that the Southern Hemisphere features are more pronounced than those of the Northern Hemisphere throughout the year and are more pronounced during the ozone hole; therefore, this section studies the Palmer Peninsula in Antarctica from August to November. The optical depth coefficients were summarized for seven heights (14.9, 18.1, 21.4, 24.6, 27.9, 31.1, and 34.4 km) (Figure 15). The high-value area changes from small to large and becomes small again in August to November, the range of high-value areas changes from small to large, and the latitude of the high-value area goes from low to high and becomes low again. The 2011 Antarctic ozone hole began to form in August, contracted and strengthened in September and October, and finally weakened in November (Figure A1) [48]. At this time, the summation diagram of the optical depth coefficients formed a high-value area within 65°S near the Palmer Peninsula in Antarctica at seven heights in August, formed a high-value area of 70°S to 80°S in September and October, and finally declined within 65°S in November. The ozone hole size was smaller in 2010 compared with 2011 [49], and the optical depth coefficients were also smaller (Figures 16 and A2).
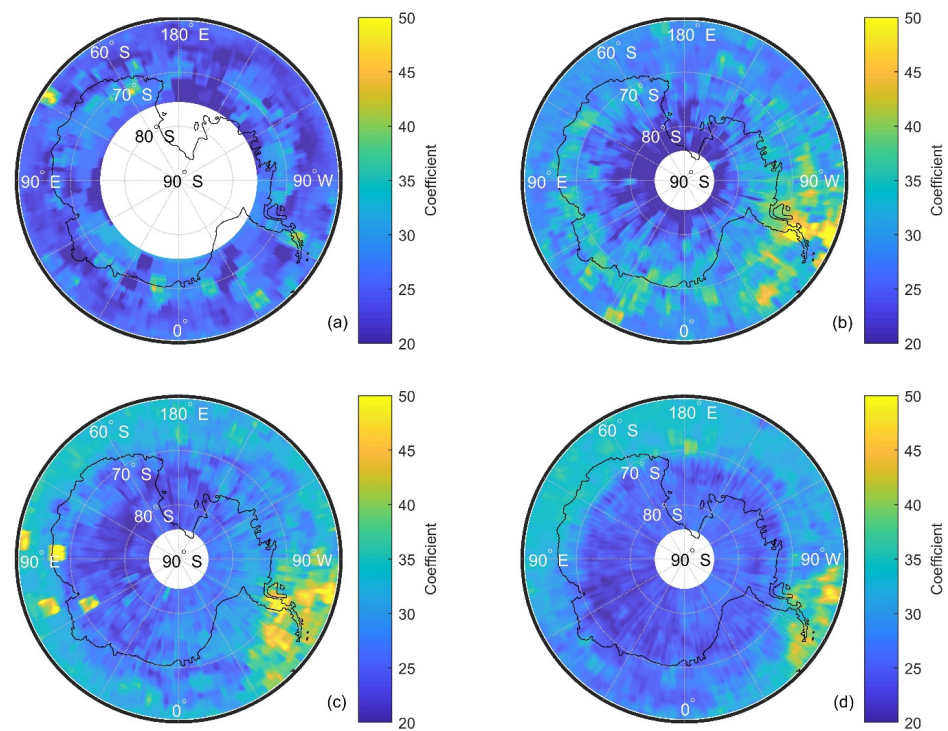
Figure 15. Summation diagrams of optical depth coefficients at 14.9, 18.1, 21.4, 24.6, 27.9, 31.1, and 34.4 km in 2011. (**a**) August, (**b**) September, (**c**) October, and (**d**) November.
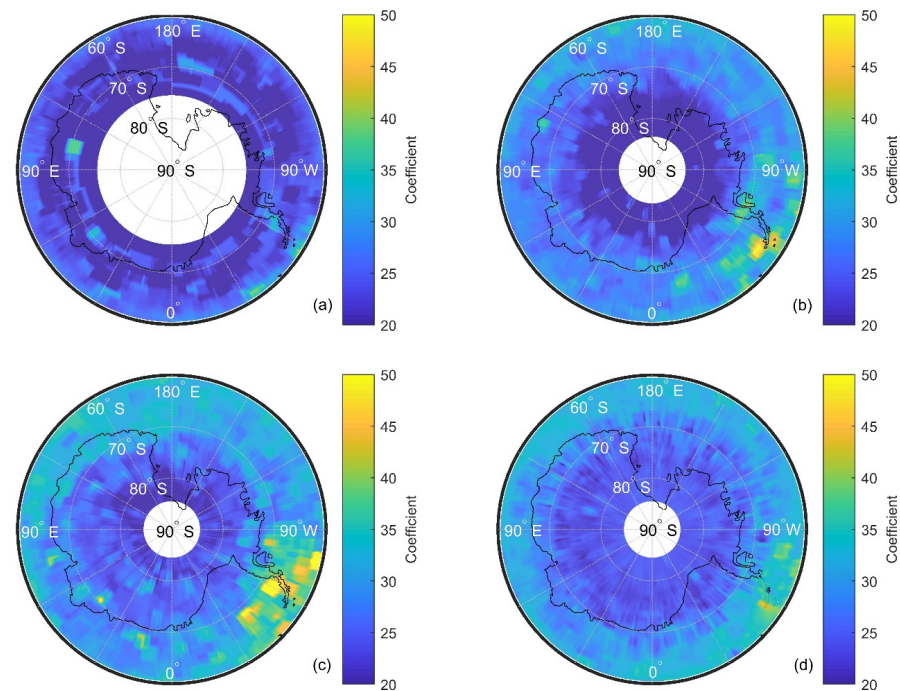
Figure 16. Summation diagrams of optical depth coefficients at 14.9, 18.1, 21.4, 24.6, 27.9, 31.1, and 34.4 km in 2010. (**a**) August, (**b**) September, (**c**) October, and (**d**) November.

The analysis of Antarctic optical depth coefficients commenced with an initial consideration of the tropopause pressure. The hypothesis was that the tropopause pressure in this region could be higher than in surrounding areas, potentially leading to an increase in the optical depth coefficients [50]. Other variables, including the sea ice extent and sea surface temperature, represent near-ground factors that should be initially considered for exclusion. There are no regions of high value near the Palmer Peninsula in Antarctica, excluding the

influence of tropopause pressure according to the NOAA global September 2010 map of tropopause pressure (Figure A3). According to NOAA's global continental shelf depth map, the Palmer Peninsula in Antarctica is closely connected to South America (Figure A4). The surface orography and land ocean contrast difference between continents and oceans affect the polar vortex [51]. The stratosphere is influenced by continental topography, particularly where the polar vortex is located. There is a substantially large global-scale impact of continental shelf depth changes on the stratosphere; however, the impact of continental shelf depth changes on the stratosphere is difficult to observe on a small scale. Compared with Northern Japan and Southwest Greenland, the anomaly region in the Palmer Peninsula exhibits more pronounced values within a more constrained range, yet it still spans a large scale of several hundred kilometers.

3.3. Relationship between Antarctic Optical Depth Coefficients and Ozone Concentration Gradient Using Statistical Methods

There is a clear correlation between the optical depth coefficients and continental shelf depth over the Palmer Peninsula in Antarctica. Initially, this area's grayscale optical depth coefficient and continental altitude were obtained (Figure 17) and histogram statistics were performed. The correlation was analyzed using the intersection method:

$$d(H_1, H_2) = \sum_I \min(H_1(I), H_2(I)) \tag{4}$$

where H_1 is the grey histogram of the continental shelf depth, H_2 is the histogram of the optical depth coefficients, and I represent the grayscale pixel.
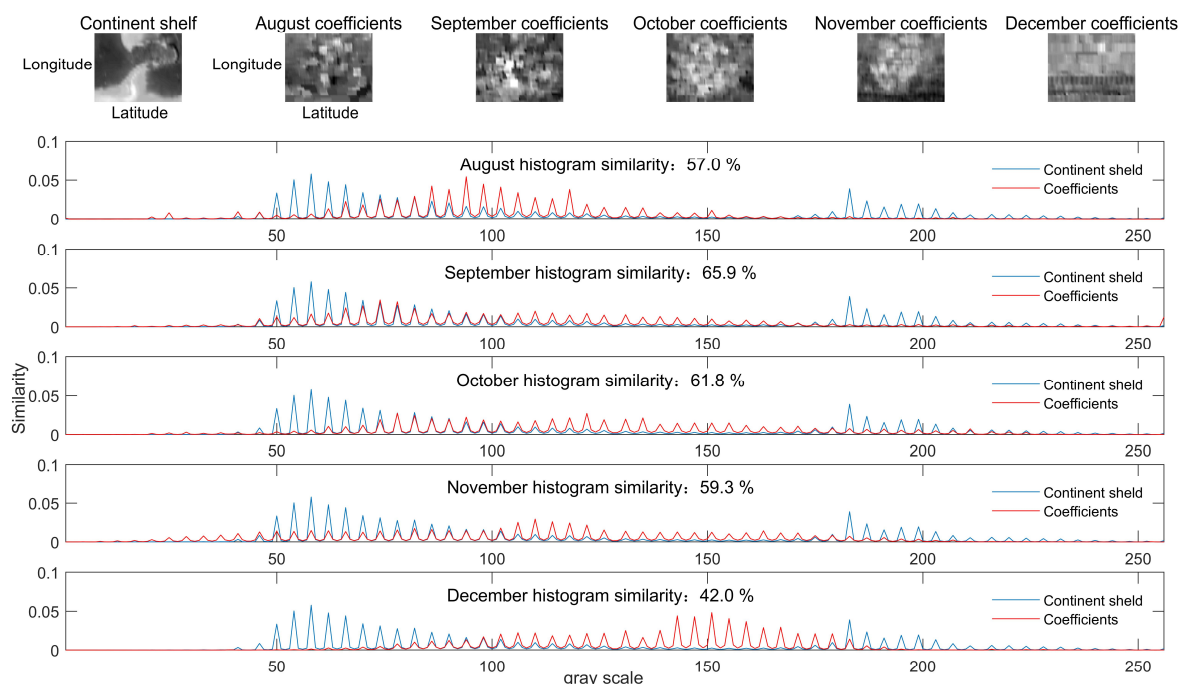
Figure 17. The similarity between the continental shelf depth and optical depth coefficients from August to December 2011.

Figure 17 shows the similarity (defined by Equation (4)) between the optical depth coefficients and continental shelf depth. The selected area is the area of the white box in Figure A4. The similarity rapidly increased from 57.01% to 65.91% from August to September; the ozone hole quickly formed, and the polar vortex became stronger. The similarity slowly decreased from 65.91% to 59.32% from September to November. Stabilization of the ozone hole establishes the polar vortex that begins to recede in late November. Finally, the similarity decreases to 41.96% in December, when the ozone hole completely dissipates

and the polar vortex flattens. Notably, the similarity in December is much lower than that in August and the coefficients in December tend to be zonally homogeneous. Therefore, the coefficient is affected by the distribution of the continental shelf depth and by the polar vortex. The above analysis explains that the anomalous increase of the optical depth coefficients is caused by the continental shelf depth change and the polar vortex's joint effect over the Antarctic Palmer Peninsula from September to November. A similar feature exists in the Northern Hemisphere north of Japan. It is weaker than Antarctica's Palmer Peninsula and even weaker in Southwestern Greenland.

4. Conclusions

The optical depth coefficients linking the Antarctic polar vortex to the continental shelf depth is a new perspective. SCIAMACHY L1 and L2 data from 2011 were used and validated using the data from 2010. The calculating method for the optical depth coefficients used in this study is the first of its type.

Optical depth coefficient heterogeneity is related to the local continental shelf depth at high latitudes; those of the Northern Hemisphere are significantly higher than those of the Southern Hemisphere, whereas the intensity distribution of heterogeneity is the opposite. Our analysis revealed that the latitudinal sea and land distributions in the high latitudes of the Southern Hemisphere were homogeneous and that a single location in the Antarctic Palmer Peninsula was heterogeneous. The Antarctic Palmer Peninsula is the only protruding part of the continental shelf depth in the high latitudes of the Southern Hemisphere (adjacent to South America); therefore, it was used as the main analysis object. The Palmer Peninsula in Antarctica is also the only area in the high latitudes of the Southern Hemisphere where the distribution of atmospheric optical depth coefficients is heterogeneous. The optical depth coefficients linked the continental shelf depth mutation to the polar vortex.

The protruding part of the continental shelf depth impacts the polar vortex. Hence, it presents a probe to directly observe the changes and strength of the polar vortex over the land and provides new ideas for observation. However, the limited sampling of limb satellite observations at different locations affected the optical depth coefficients' resolutions. Future work will involve the synthesis of more limb satellite data results to form finer optical depth coefficients and evaluate the effects of continental shelf depth protrusions on polar vortices in this region in detail. This study's optical depth coefficient calculations are based on the ozone density. However, the final result is not directly related to the ozone density. Similarly, the optical depth coefficients for other atmospheric gases can be theoretically derived to determine if they enhance performance. The factors influencing the impact of continental shelf depth on optical depth coefficients have yet to be explored in depth.

Author Contributions: Z.X.: Conceptualization, Methodology, Software, Validation, Formal analysis, Investigation, Writing—original draft, Visualization, Resources. Y.Q.: Software, Formal analysis. T.Y.: Software, Formal analysis. F.T.: Resources. Y.L.: Formal analysis. F.S.: Methodology, Funding acquisition, Writing—review and editing. All authors have read and agreed to the published version of the manuscript.

Data Availability Statement: The data used in this study are available on request. QDOAS software: https://atmospherictoolbox.org/qdoas/, accessed on 15 June 2022. SCIAMACHYL1B data: https://earth.esa.int/, accessed on 15 June 2022. NOAA data: https://www.noaa.gov/, accessed on 15 June 2021.

Appendix A
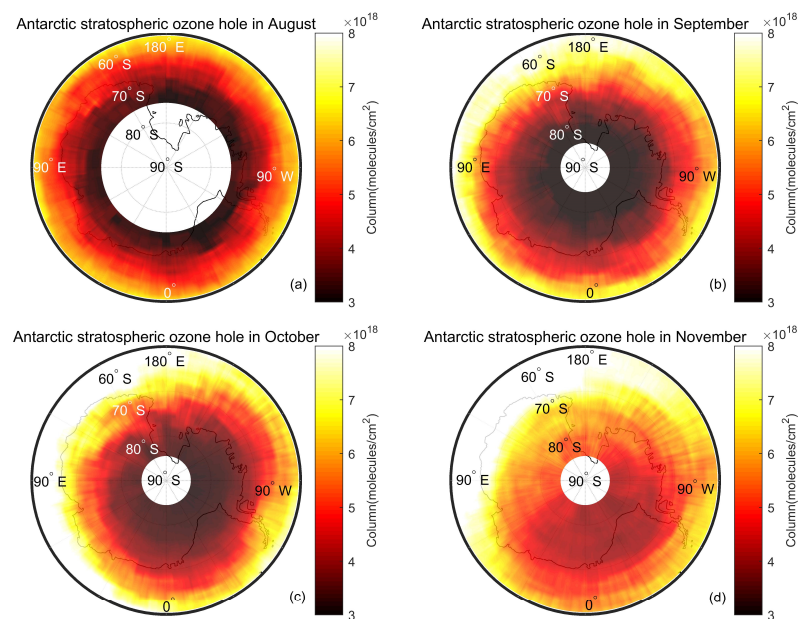
Figure A1. Map of the Antarctic stratospheric ozone hole in 2011. (**a**) August, (**b**) September, (**c**) October, and (**d**) November.
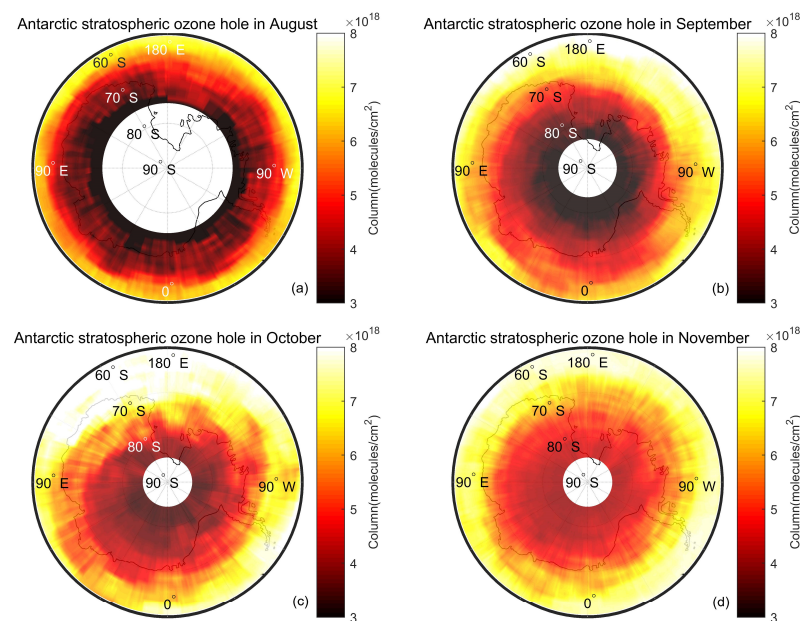
Figure A2. Map of the Antarctic stratospheric ozone hole in 2010. (**a**) August, (**b**) September, (**c**) October, and (**d**) November.
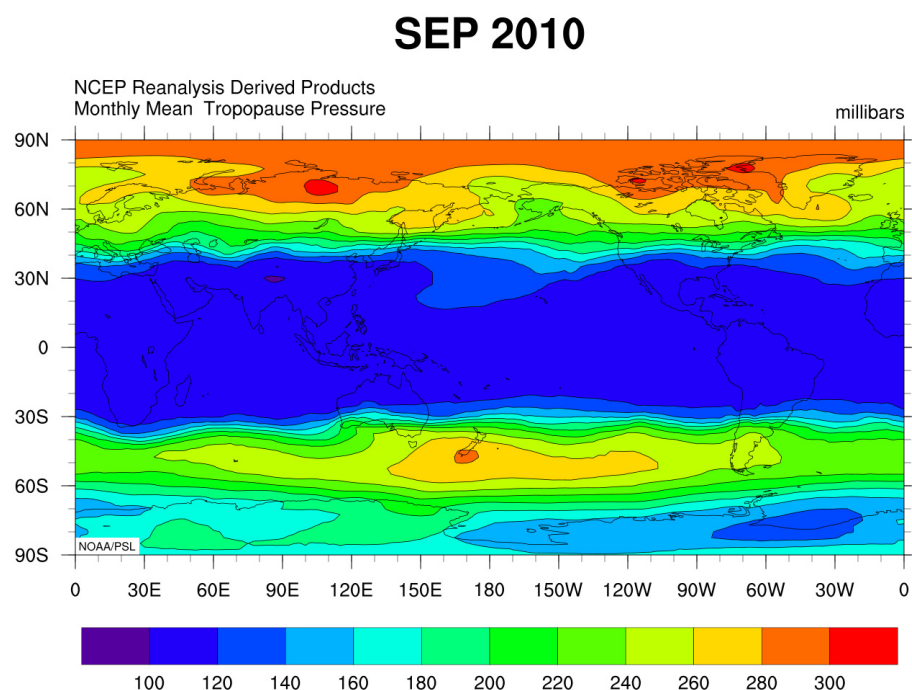
Figure A3. National Oceanic and Atmospheric Administration (NOAA) map of tropopause pressure in September 2010 (https://psl.noaa.gov/mddb2/makePlot.html?variableID=155611, accessed on 11 January 2023).
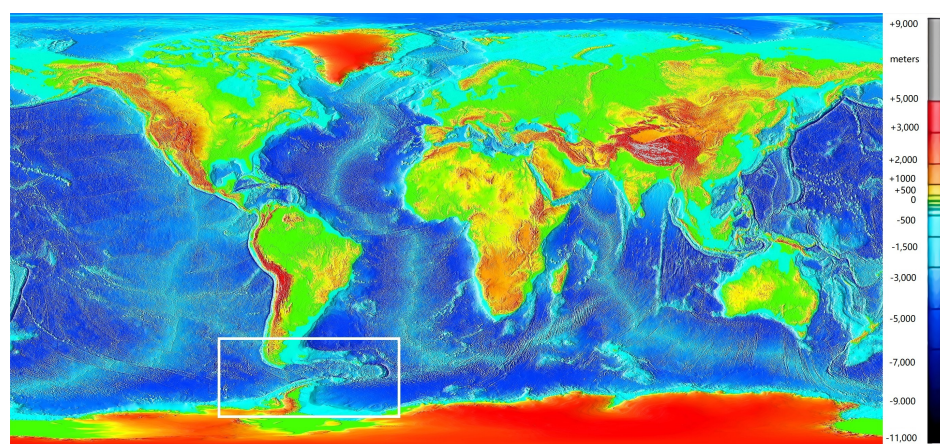
Figure A4. NOAA map of world continental shelf depth (http://www.ngdc.noaa.gov/mgg/image/2minrelief.html, accessed on 11 January 2023).

References

1. Sofieva, V.F.; Tamminen, J.; Kyrölä, E.; Mielonen, T.; Veefkind, P.; Hassler, B.; Bodeker, G.E. A novel tropopause-related climatology of ozone profiles. *Atmos. Chem. Phys.* **2014**, *14*, 283–299. [CrossRef]
2. Kuttippurath, J.; Kumar, P.; Nair, P.J.; Chakraborty, A. Accuracy of satellite total column ozone measurements in polar vortex conditions: Comparison with ground-based observations in 1979–2013. *Remote Sens. Environ.* **2018**, *209*, 648–659. [CrossRef]
3. Dhomse, S.S.; Kinnison, D.; Chipperfield, M.P.; Salawitch, R.J.; Cionni, I.; Hegglin, M.I.; Zeng, G. Estimates of ozone return dates from Chemistry-Climate Model Initiative simulations. *Atmos. Chem. Phys.* **2018**, *18*, 8409–8438. [CrossRef]
4. Meul, S.; Dameris, M.; Langematz, U.; Abalichin, J.; Kerschbaumer, A.; Kubin, A.; Oberländer-Hayn, S. Impact of rising greenhouse gas concentrations on future tropical ozone and UV exposure. *Geophys. Res. Lett.* **2016**, *43*, 2919–2927. [CrossRef]
5. Fang, X.; Pyle, J.A.; Chipperfield, M.P.; Daniel, J.S.; Park, S.; Prinn, R.G. Challenges for the recovery of the ozone layer. *Nat. Geosci.* **2019**, *12*, 592–596. [CrossRef]
6. Montzka, S.A.; Dutton, G.S.; Yu, P.; Ray, E.; Portmann, R.W.; Daniel, J.S.; Elkins, J.W. An unexpected and persistent increase in global emissions of ozone-depleting CFC-11. *Nature* **2018**, *557*, 413–417. [CrossRef]

7. Wohltmann, I.; von der Gathen, P.; Lehmann, R.; Maturilli, M.; Deckelmann, H.; Manney, G.L.; Rex, M. Near-complete local reduction of Arctic stratospheric ozone by severe chemical loss in spring 2020. *Geophys. Res. Lett.* **2020**, *47*, e2020GL089547. [CrossRef]

8. Solomon, S.; Garcia, R.R.; Rowland, F.S.; Wuebbles, D.J. On the depletion of Antarctic ozone. *Nature* **1986**, *321*, 755–758. [CrossRef]

9. Wargan, K.; Kramarova, N.; Weir, B.; Pawson, S.; Davis, S.M. Toward a reanalysis of stratospheric ozone for trend studies: Assimilation of the aura microwave limb sounder and ozone mapping and profiler suite limb profiler data. *J. Geophys. Res. Atmos.* **2020**, *125*, e2019JD031892. [CrossRef]

10. Charney, J.G.; Drazin, P.G. Propagation of planetary-scale disturbances from the lower into the upper atmosphere. *J. Geophys. Res.* **1961**, *66*, 83–109. [CrossRef]

11. Conway, J.; Bodeker, G.; Cameron, C. Bifurcation of potential vorticity gradients across the Southern Hemisphere stratospheric polar vortex. *Atmos. Chem. Phys.* **2018**, *18*, 8065–8077. [CrossRef]

12. Varotsos, C.A.; Cracknell, A.P. Remote sounding of minor constituents in the stratosphere and heterogeneous reactions of gases at solid interfaces. *Int. J. Remote Sens.* **1994**, *15*, 1525–1530. [CrossRef]

13. Varotsos, C.A.; Zellner, R. A new modeling tool for the diffusion of gases in ice or amorphous binary mixture in the polar stratosphere and the upper troposphere. *Atmos. Chem. Phys.* **2010**, *10*, 3099–3105. [CrossRef]

14. Matsuno, T. Vertical propagation of stationary planetary waves in the winter Northern Hemisphere. *J. Atmos. Sci.* **1970**, *27*, 871–883. [CrossRef]

15. Waugh, D.W.; Randel, W.J. Climatology of Arctic and Antarctic polar vortices using elliptical diagnostics. *J. Atmos. Sci.* **1999**, *56*, 1594–1613. [CrossRef]

16. Waugh, D.W.; Polvani, L.M. The Stratosphere: Dynamics, Transport, and Chemistry. *Geophys. Monogr. Ser.* **2010**, *190*, 43–57.

17. Waugh, D.W.; Sobel, A.H.; Polvani, L.M. What is the polar vortex and how does it influence weather? *Bull. Am. Meteorol. Soc.* **2017**, *98*, 37–44. [CrossRef]

18. Newman, P.A.; Kawa, S.R.; Nash, E.R. On the size of the Antarctic ozone hole. *Geophys. Res. Lett.* **2004**, *31*, 21. [CrossRef]

19. Domeisen, D.I.; Butler, A.H. Stratospheric drivers of extreme events at the Earth's surface. *Commun. Earth Environ.* **2020**, *1*, 59. [CrossRef]

20. Manney, G.L.; Livesey, N.J.; Santee, M.L.; Froidevaux, L.; Lambert, A.; Lawrence, Z.D.; Fuller, R.A. Record-low Arctic stratospheric ozone in 2020: MLS observations of chemical processes and comparisons with previous extreme winters. *Geophys. Res. Lett.* **2020**, *47*, e2020GL089063. [CrossRef]

21. Domeisen, D.I.; Martius, O.; Jiménez-Esteve, B. Rossby wave propagation into the Northern Hemisphere stratosphere: The role of zonal phase speed. *Geophys. Res. Lett.* **2018**, *45*, 2064–2071. [CrossRef]

22. Gonsamo, A.; Chen, J.M. Circumpolar vegetation dynamics product for global change study. *Remote Sens. Environ.* **2016**, *182*, 13–26. [CrossRef]

23. Damiani, A.; De Simone, S.; Rafanelli, C.; Cordero, R.R.; Laurenza, M. Three years of ground-based total ozone measurements in the Arctic: Comparison with OMI, GOME and SCIAMACHY satellite data. *Remote Sens. Environ.* **2012**, *127*, 162–180. [CrossRef]

24. Butchart, N. The Brewer-Dobson circulation. *Rev. Geophys.* **2014**, *52*, 157–184. [CrossRef]

25. Weber, M.; Dikty, S.; Burrows, J.P.; Garny, H.; Dameris, M.; Kubin, A.; Langematz, U. The Brewer-Dobson circulation and total ozone from seasonal to decadal time scales. *Atmos. Chem. Phys.* **2011**, *11*, 11221–11235. [CrossRef]

26. Phanikumar, D.V.; Kumar, K.N.; Bhattacharjee, S.; Naja, M.; Girach, I.A.; Nair, P.R.; Kumari, S. Unusual enhancement in tropospheric and surface ozone due to orography induced gravity waves. *Remote Sens. Environ.* **2017**, *199*, 256–264. [CrossRef]

27. Fusco, A.C.; Salby, M.L. Interannual variations of total ozone and their relationship to variations of planetary wave activity. *J. Clim.* **1999**, *12*, 1619–1629. [CrossRef]

28. Auvinen, H.; Oikarinen, L.; Kyrölä, E. Inversion algorithms for recovering minor species densities from limb scatter measurements at UV-visible wavelengths. *J. Geophys. Res. Atmos.* **2002**, *107*, ACH-7. [CrossRef]

29. Rohen, G.J.; von Savigny, C.; Llewellyn, E.J.; Kaiser, J.W.; Eichmann, K.U.; Bracher, A.; Burrows, J.P. First results of ozone profiles between 35 and 65 km retrieved from SCIAMACHY limb spectra and observations of ozone depletion during the solar proton events in October/November 2003. *Adv. Space Res.* **2006**, *37*, 2263–2268. [CrossRef]

30. Corsmeier, U.; Kohler, M.; Vogel, B.; Vogel, H.; Fiedler, F. BAB II: A project to evaluate the accuracy of real-world traffic emissions for a motorway. *Atmos. Environ.* **2005**, *39*, 5627–5641. [CrossRef]

31. Verkruysse, W.; Todd, L.A. Improved method "grid translation" for mapping environmental pollutants using a two-dimensional CAT scanning system. *Atmos. Environ.* **2004**, *38*, 1801–1809. [CrossRef]

32. Pundt, I.; Mettendorf, K.U. Multibeam long-path differential optical absorption spectroscopy instrument: A device for simultaneous measurements along multiple light paths. *Appl. Opt.* **2005**, *44*, 4985–4994. [CrossRef]

33. Pundt, I. DOAS tomography for the localisation and quantification of anthropogenic air pollution. *Anal. Bioanal. Chem.* **2006**, *385*, 18–21. [CrossRef] [PubMed]

34. Hönninger, G.; Von Friedeburg, C.; Platt, U. Multi axis differential optical absorption spectroscopy (MAX-DOAS). *Atmos. Chem. Phys.* **2004**, *4*, 231–254. [CrossRef]

35. Laepple, T.; Knab, V.; Mettendorf, K.U.; Pundt, I. Longpath DOAS tomography on a motorway exhaust gas plume: Numerical studies and application to data from the BAB II campaign. *Atmos. Chem. Phys.* **2004**, *4*, 1323–1342. [CrossRef]

36. Zhu, F.; Si, F.; Zhou, H.; Dou, K.; Zhao, M.; Zhang, Q. Sensitivity Analysis of Ozone Profiles Retrieved from SCIAMACHY Limb Radiance Based on the Weighted Multiplicative Algebraic Reconstruction Technique. *Remote Sens.* **2022**, *14*, 3954. [CrossRef]
37. Livesey, N.J.; Van Snyder, W.; Read, W.G.; Wagner, P.A. Retrieval algorithms for the EOS Microwave limb sounder (MLS). *IEEE Trans. Geosci. Remote Sens.* **2006**, *44*, 1144–1155. [CrossRef]
38. Bovensmann, H.; Burrows, J.P.; Buchwitz, M.; Frerick, J.; Noël, S.; Rozanov, V.V.; Goede, A.P.H. SCIAMACHY: Mission objectives and measurement modes. *J. Atmos. Sci.* **1999**, *56*, 127–150. [CrossRef]
39. Hu, Y.; Yan, H.; Zhang, X.; Gao, Y.; Zheng, X.; Liu, X. Study on calculation and validation of tropospheric ozone by ozone monitoring instrument–microwave limb sounder over China. *Int. J. Remote Sens.* **2020**, *41*, 9101–9120. [CrossRef]
40. Qian, Y.; Luo, Y.; Si, F.; Zhou, H.; Yang, T.; Yang, D.; Xi, L. Total Ozone Columns from the Environmental Trace Gases Monitoring Instrument (EMI) Using the DOAS Method. *Remote Sens.* **2021**, *13*, 2098. [CrossRef]
41. Qian, Y.; Luo, Y.; Dou, K.; Zhou, H.; Xi, L.; Yang, T.; Si, F. Retrieval of tropospheric ozone profiles using ground-based MAX-DOAS. *Sci. Total Environ.* **2023**, *857*, 159341. [CrossRef] [PubMed]
42. Wang, Z.; Chen, S.; Jin, L.; Yang, C. Ozone profiles retrieval from SCIAMACHY Chappuis-Wulf limb scattered spectra using MART. *Sci. China Phys. Mech. Astron.* **2011**, *54*, 273–280. [CrossRef]
43. Loughman, R.P.; Flittner, D.E.; Herman, B.M.; Bhartia, P.K.; Hilsenrath, E.; McPeters, R.D. Description and sensitivity analysis of a limb scattering ozone retrieval algorithm. *J. Geophys. Res. Atmos.* **2005**, *110*, D19. [CrossRef]
44. Rahpoe, N.; Von Savigny, C.; Weber, M.; Rozanov, A.V.; Bovensmann, H.; Burrows, J.P. Error budget analysis of SCIAMACHY limb ozone profile retrievals using the SCIATRAN model. *Atmos. Meas. Tech.* **2013**, *6*, 2825–2837. [CrossRef]
45. Bourassa, A.E.; Degenstein, D.A.; Gattinger, R.L.; Llewellyn, E.J. Stratospheric aerosol retrieval with optical spectrograph and infrared imaging system limb scatter measurements. *J. Geophys. Res. Atmos.* **2007**, *112*, D10. [CrossRef]
46. Corazza, E.; Tesi, G. Tropospheric hydrogen and carbon oxides in Antarctica and in Greenland. *Sci. Total Environ.* **1995**, *160*, 803–809. [CrossRef]
47. Kovář, P.; Sommer, M. CubeSat Observation of the Radiation Field of the South Atlantic Anomaly. *Remote Sens.* **2021**, *13*, 1274. [CrossRef]
48. Zuev, V.V.; Savelieva, E. Antarctic polar vortex dynamics during spring 2002. *J. Earth Syst. Sci.* **2022**, *131*, 119. [CrossRef]
49. Shen, X.; Wang, L.; Osprey, S.; Hardiman, S.C.; Scaife, A.A.; Ma, J. The life cycle and variability of Antarctic weak polar vortex events. *J. Clim.* **2022**, *35*, 2075–2092. [CrossRef]
50. Kang, D.; Im, J.; Lee, M.I.; Quackenbush, L.J. The MODIS ice surface temperature product as an indicator of sea ice minimum over the Arctic Ocean. *Remote Sens. Environ.* **2014**, *152*, 99–108. [CrossRef]
51. Mitchell, D.M.; Scott, R.K.; Seviour, W.J.; Thomson, S.I.; Waugh, D.W.; Teanby, N.A.; Ball, E.R. Polar vortices in planetary atmospheres. *Rev. Geophys.* **2021**, *59*, e2020RG000723. [CrossRef]